

PTYCHOGRAPHIC AMBIGUITY AND RECONSTRUCTION

ALBERT FANNJIANG AND ZHEQING ZHANG

ABSTRACT. Blind ptychography is the scanning version of coherent diffractive imaging which seeks to recover both the object and the probe are simultaneously. Concrete examples of ambiguity in blind ptychography are presented to illustrate the challenge of blind ptychography. Two opposing classes of measurement schemes are discussed: the mixing schemes and the raster scans. The former generally admit only a complex scaling factor and a linear phase ambiguity as ambiguities while the latter a host of other ambiguities of many degrees of freedom.

AMDRS is a reconstruction algorithm based on alternating minimization by Douglas-Rachford splitting. Enabled by an initialization method informed by the probe phase constraint in the theory of uniqueness, AMDRS converges globally and geometrically. The technique of bright-field boundary condition is introduced to remove the linear phase ambiguity and accelerate convergence, and the technique of adding salt noise is used to improve the quality of reconstruction of objects exhibiting extensive area of dark pixels.

1. INTRODUCTION

Ptychography is the scanning version of coherent diffractive imaging (CDI) [9] that acquires multiple diffraction patterns through the scan of a localized illumination on an extended object (Fig. 1). The redundant information in the overlap between adjacent illuminated spots is then exploited to improve phase retrieval methods [46, 49]. Ptychography originated in electron microscopy [22, 26, 27, 31, 44, 45, 50] and has been successfully implemented with X-ray, optical and terahertz waves [14, 20, 51, 52, 54, 57, 58, 61].

An important feature of ptychography developed in Thibault *et al.* [57, 58] is simultaneous recovery of the object and the probe. This capability allows application of ptychography as a beam characterization and wave front aberration sensing technique.

Recently ptychography has been extended to the Fourier domain [47, 68]. In Fourier ptychography, illumination angles are scanned sequentially with a programmable array source with the diffraction pattern measured at each angle [34, 60]. Tilted illumination samples different regions of Fourier space, as in synthetic-aperture and structured-illumination imaging.

Yet, despite significant progress that allows for reliable practical implementation, some of the technique's fundamentals remain poorly understood [12]. For example, precise conditions for uniqueness of solution are not known until recently. For standard nonptychographic phase retrieval, it has long be established that a randomly selected object (i.e. generic object) can be uniquely determined up to the trivial ambiguities, including a constant phase factor, a global translation and the twin image [4, 5, 25]. With a randomly structured illumination, all ambiguities but the constant phase factor can be eliminated for all (not just generic) objects [17].

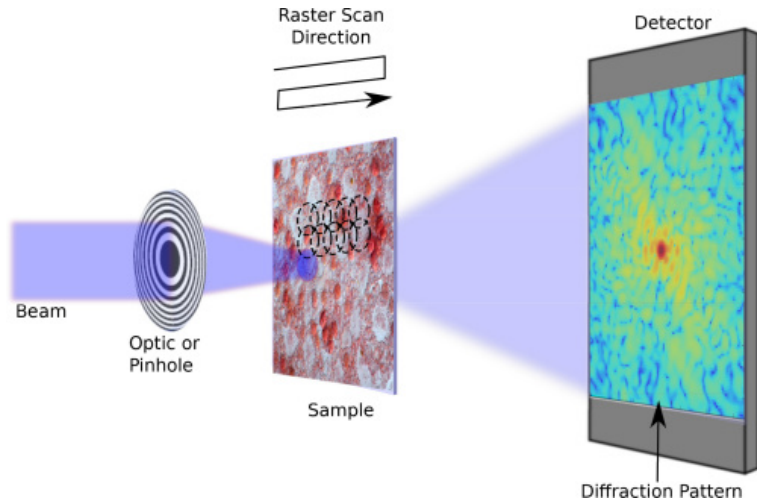


FIGURE 1. Simplified ptychographic setup showing a Cartesian grid used for the overlapping raster scan positions [43].

On the other hand, to our knowledge, such a theory is not available for ptychographic phase retrieval until recently [18]. In contrast to standard phase retrieval, ptychographic reconstruction can not resolve a constant scaling factor and an affine phase ramp (provided that the locations of the probe are known) [37]. Under what conditions are these only ptychographic ambiguities? Are there other types of ptychographic ambiguity? In the present work we systematically discuss these questions in the context of randomly structured illumination and present noise-robust reconstruction algorithms. We emphasize how these ambiguities and the choice of structured illuminations, sampling schemes and objective functions affect ptychographic reconstruction.

Roughly speaking the uniqueness theory [18] says that for a general class of non-raster scan schemes, called the mixing schemes (Section 4), a constant scaling and an affine phase ramp are the only ptychographic ambiguities with the use of a randomly phased probe.

On the other hand, when the prior information about the object support is too weak, other forms of ambiguity can emerge, including parts of the object forming twin-like images and being shifted in different directions (Section 3). And specially for raster scan there are the periodic ambiguity and the phase drift ambiguity of many degrees of freedom (Section 5).

The purpose of this work is to precisely formulate examples to demonstrate the uniqueness results in [18] and present a reconstruction algorithm whose performance closely tracks the mathematical conditions therein.

1.1. Notation and setup. We adopt the following notations in the paper. Let the $n \times n$ integer lattice \mathbb{Z}_n^2 be the object domain containing the support of the discrete object f . Without loss of generality, let $\mathcal{M}^0 := \mathbb{Z}_m^2$ be the initial probe region with the structured illumination given by μ^0 .

Let \mathcal{T} be the set of all shifts, including $(0, 0)$, involved in the ptychographic measurement. For general ptychographic schemes, we denote by $\mu^{\mathbf{t}}$ the \mathbf{t} -shifted probe for all $\mathbf{t} \in \mathcal{T}$ and $\mathcal{M}^{\mathbf{t}}$ the domain of $\mu^{\mathbf{t}}$. Let $f^{\mathbf{t}}$ the object restricted to $\mathcal{M}^{\mathbf{t}}$ and $\text{Twin}(f^{\mathbf{t}})$ the twin image of $f^{\mathbf{t}}$ defined in $\mathcal{M}^{\mathbf{t}}$. Let $\text{supp}(f) \subseteq \bigcup_{\mathbf{t} \in \mathcal{T}} \mathcal{M}^{\mathbf{t}}$ and write $f = \bigcup_{\mathbf{t} \in \mathcal{T}} f^{\mathbf{t}}$ where $f^{\mathbf{t}}$ is the restriction of f to $\mathcal{M}^{\mathbf{t}}$.

In the case of raster scan \mathcal{T} consists of $\mathbf{t}_{kl} := \tau(k, l), k, l = 0, \dots, q - 1$, with a constant stepsize $\tau \in \mathbb{N}$. Although the raster scan is prone to the periodic artifacts called the raster grid pathology, it serves as the basis of the more useful mixing schemes discussed in Section 4. For convenience we set $\tau = n/q, q \in \mathbb{N}$ and impose the periodic boundary condition on \mathbb{Z}_n^2 so that every object pixel is covered by the same number of shifted probes during the ptychographic measurement. The periodic boundary condition means that the shifted probe is wrapped around into the other end of the object domain. Denote the \mathbf{t}_{kl} -shifted probes and blocks by μ^{kl} and \mathcal{M}^{kl} , respectively. Likewise, denote by f^{kl} the object restricted to the shifted domain \mathcal{M}^{kl} .

The more useful and practical schemes are the non-raster-scanning schemes, called the mixing schemes. Examples of the mixing schemes include randomly perturbed raster scans consisting of

$$(1) \quad \mathbf{t}_{kl} = \tau(k, l) + (\delta_k^1, \delta_l^2),$$

where δ_k^1, δ_l^2 are small, randomly distributed integers, or

$$(2) \quad \mathbf{t}_{kl} = \tau(k, l) + (\delta_{kl}^1, \delta_{kl}^2),$$

where $\delta_{kl}^1, \delta_{kl}^2$ are small, randomly distributed integers.

For the randomly phased probe, we will focus on the effect of *random phase* θ in the probe function $\mu^0(\mathbf{n}) = |\mu^0(\mathbf{n})|e^{i\theta(\mathbf{n})}$ where $\theta(\mathbf{n})$ are independent, continuous real-valued random variables and $|\mu^0(\mathbf{n})| \neq 0, \forall \mathbf{n} \in \mathcal{M}^0$. Randomly phased probes have been adopted in ptychographic experiments [38, 42].

A fundamental prior in our approach is the probe phase constraint (PPC): *We say that a probe estimate ν^0 satisfies PPC with $\delta < 1$ if*

$$(3) \quad \angle(\nu^0(\mathbf{n}), \mu^0(\mathbf{n})) < \delta\pi, \quad \forall \mathbf{n}.$$

The default case is $\delta = 1/2$ and PPC has the intuitive meaning $\Re(\bar{\nu}^0 \odot \mu^0) > 0$ at every pixel (where \odot denotes the component-wise product, the bar the complex conjugate and \Re the real part).

As shown in our numerical experiments, PPC is useful and effective for selecting initial guess for probe estimate.

2. BLOCK PHASE AMBIGUITY

First recall the affine phase ambiguity, a basic form of ptychographic ambiguity. Let ν^0 and g be the probe and the object estimates that produce the same ptychographic measurement

data as μ^0 and f . Let $\nu^0(\mathbf{n}) = \mu^0(\mathbf{n}) \exp(-i\mathbf{w} \cdot \mathbf{n})$ for some $\mathbf{w} \in \mathbb{R}^2$. Let $g(\mathbf{n}) = f(\mathbf{n}) \exp(i\mathbf{w} \cdot \mathbf{n})$. For any \mathbf{t} , we have the following calculation

$$\begin{aligned}\nu^{\mathbf{t}}(\mathbf{n}) &= \nu^0(\mathbf{n} - \mathbf{t}) \\ &= \mu^0(\mathbf{n} - \mathbf{t}) \exp(-i\mathbf{w} \cdot (\mathbf{n} - \mathbf{t})) \\ &= \mu^{\mathbf{t}}(\mathbf{n}) \exp(-i\mathbf{w} \cdot (\mathbf{n} - \mathbf{t})).\end{aligned}$$

Since, by the above calculation,

$$(4) \quad \nu^{\mathbf{t}}(\mathbf{n})g^{\mathbf{t}}(\mathbf{n}) = \mu^{\mathbf{t}}(\mathbf{n})f^{\mathbf{t}}(\mathbf{n}) \exp(i\mathbf{w} \cdot \mathbf{t}), \quad \forall \mathbf{n}, \mathbf{t},$$

g and $\nu^{\mathbf{t}}$ produce the same diffraction pattern as f and $\mu^{\mathbf{t}}$.

Motivated by (4), we seek the conditions under which the following relationship holds:

$$(5) \quad \nu^{\mathbf{t}} \odot g^{\mathbf{t}} = e^{i\theta_{\mathbf{t}}} \mu^{\mathbf{t}} \odot f^{\mathbf{t}}, \quad \mathbf{t} \in \mathcal{T}, \quad \theta_{\mathbf{t}} \in \mathbb{R},$$

where $\theta_{\mathbf{t}}$ is constant in each block but can vary from block to block. We call $\theta_{\mathbf{t}}$ the block phase. Eq. (4) shows that the affine profile $\theta_{\mathbf{t}} = \theta_0 + \mathbf{w} \cdot \mathbf{t}$ is always a possibility. Can there be other possibilities? Under what conditions is the affine phase profile the only possibility? In what follows we give partial answers to these questions.

Roughly speaking, uniqueness theory in [18] asserts that (5) holds with high probability for any strongly connected object under PPC and certain object support constraint (e.g. for at least one $\mathbf{s} \in \mathcal{T}$, $f^{\mathbf{s}}$ has a tight support in $\mathcal{M}^{\mathbf{s}}$). Here the high probability refers to the selection of random probe. And we say that the set of parts $\{f^{\mathbf{t}} : \mathbf{t} \in \mathcal{T}\}$ is strongly connected if any two parts are joined by a chain in which two successive parts $f^{\mathbf{t}}, f^{\mathbf{t}'}$ overlap in the following sense:

$$(6) \quad \min \left\{ |\mathcal{M}^{\mathbf{t}} \cap \mathcal{M}^{\mathbf{t}'} \cap \text{supp}(f^{\mathbf{t}})|, |\mathcal{M}^{\mathbf{t}} \cap \mathcal{M}^{\mathbf{t}'} \cap \text{supp}(\text{Twin}(f^{\mathbf{t}}))| \right\} \gg 1,$$

where $|\cdot|$ denotes the cardinality of the set.

3. AMBIGUITIES WITH LOOSE SUPPORT

Objects of loose support can create ptychographic ambiguities other than a constant scaling factor and an affine phase factor. Further, (5) may be altogether untenable for loose support in general. Although the following examples involve ptychographic measurements with only two diffraction patterns, more elaborate examples can be constructed and omitted for simplicity of presentation. The important feature of the examples is that besides loose support the object values are arbitrary.

Example 3.1. For $m = 3n/5$ consider $\mathcal{T} = \{(0, 0), \mathbf{t}\}$ where $\mathbf{t} = (2m/3, 0)$. Evenly partition f^0 and $f^{\mathbf{t}}$ into three $m \times m/3$ parts as $f^0 = [0, f_1^0, f_2^0]$ and $f^{\mathbf{t}} = [f_0^1, f_1^1, 0]$ with the overlap $f_2^0 = f_0^1$. Likewise, partition the probe as $\mu^0 = [\mu_0^0, \mu_1^0, \mu_2^0]$, $\mu^{\mathbf{t}} = [\mu_0^1, \mu_1^1, \mu_2^1]$ where $\mu^{\mathbf{t}}$ is just the \mathbf{t} -shift of μ^0 , i.e. $\mu^{\mathbf{t}}(\mathbf{n} + \mathbf{t}) = \mu^0(\mathbf{n})$.

Let $\nu^0 = \mu^0$, $\nu^{\mathbf{t}} = \mu^{\mathbf{t}}$ and $g^0 = [g_0^0, g_1^0, 0]$, $g^{\mathbf{t}} = [0, g_1^1, g_2^1]$ where

$$(7) \quad g_0^0 = f_1^0 \odot \mu_1^0 / \mu_0^0, \quad g_1^0 = f_2^0 \odot \mu_2^0 / \mu_1^0$$

$$(8) \quad g_1^1 = f_0^1 \odot \mu_0^1 / \mu_1^1, \quad g_2^1 = f_1^1 \odot \mu_1^1 / \mu_2^1.$$

Clearly, $g = [g_0^0, g_1^0, 0, g_1^1, g_2^1]$ is different from $f = [0, f_1^0, f_2^0, f_1^1, 0]$.

It is straightforward to check that for $\mathbf{m} = (m/3, 0)$

$$(9) \quad g^0(\mathbf{n})\nu^0(\mathbf{n}) = f^0(\mathbf{n} + \mathbf{m})\mu^0(\mathbf{n} + \mathbf{m}), \quad \mathbf{n} \in \mathcal{M}^0$$

$$(10) \quad g^{\mathbf{t}}(\mathbf{n})\nu^{\mathbf{t}}(\mathbf{n}) = f^{\mathbf{t}}(\mathbf{n} - \mathbf{m})\mu^{\mathbf{t}}(\mathbf{n} - \mathbf{m}), \quad \mathbf{n} \in \mathcal{M}^{\mathbf{t}}$$

and hence $g^0 \odot \mu^0$ and $g^{\mathbf{t}} \odot \mu^{\mathbf{t}}$ produce the same diffraction patterns as $f^0 \odot \mu^0$ and $f^{\mathbf{t}} \odot \mu^{\mathbf{t}}$.

On the other hand, $g^0(\mathbf{n})\nu^0(\mathbf{n}) \neq e^{i\theta_0} f^0(\mathbf{n})\mu^0(\mathbf{n})$ and $g^{\mathbf{t}}(\mathbf{n})\nu^{\mathbf{t}}(\mathbf{n}) \neq e^{i\theta_{\mathbf{t}}} f^{\mathbf{t}}(\mathbf{n})\mu^{\mathbf{t}}(\mathbf{n})$ in general. Hence (5) is violated.

The ambiguity in Example 3.1 is due to a loose object support which can also produce the ambiguity of conjugate inversion as follows.

Example 3.2. For $m = n$ consider $\mathcal{T} = \{(0, 0), \mathbf{t}\}$ where $\mathbf{t} = (m/2, 0)$ with the periodic boundary condition. Evenly partition f^0 and $f^{\mathbf{t}}$ into two $m \times m/2$ parts as $f^0 = [0, f_1^0]$ and $f^{\mathbf{t}} = [f_0^1, 0]$ with the overlap $f_1^0 = f_0^1$. Likewise, partition the probe as $\mu^0 = [\mu_0^0, \mu_1^0]$, $\mu^{\mathbf{t}} = [\mu_0^1, \mu_1^1]$ where $\mu^{\mathbf{t}}(\mathbf{n} + \mathbf{t}) = \mu^0(\mathbf{n})$.

Let $\nu^0 = \mu^0, \nu^{\mathbf{t}} = \mu^{\mathbf{t}}$ and $g^0 = [g_0^0, 0], g^{\mathbf{t}} = [0, g_1^1]$ where

$$(11) \quad g_0^0(\mathbf{n}) = \bar{f}_1^0(\mathbf{N} - \mathbf{n})\bar{\mu}_1^0(\mathbf{N} - \mathbf{n})/\mu_0^0(\mathbf{n})$$

$$(12) \quad g_1^1(\mathbf{n}) = \bar{f}_0^1(\mathbf{N} - \mathbf{n})\bar{\mu}_0^1(\mathbf{N} - \mathbf{n})/\mu_1^1(\mathbf{n}).$$

In other words, $g = [g_0^0, 0, g_1^1]$ is the twin-like image of $f = [0, f_1^1, 0]$. Since $2\mathbf{t} = (m, 0) = (0, 0)$ under the periodic boundary condition, we have $g_0^0 = g_1^1$. So the construction (11)-(12) is consistent with the periodic boundary condition.

Setting $\nu^0 = \mu^0$ we have

$$\begin{aligned} g^0(\mathbf{n})\nu^0(\mathbf{n}) &= \bar{f}^0(\mathbf{N} - \mathbf{n})\bar{\mu}^0(\mathbf{N} - \mathbf{n}) \\ g^{\mathbf{t}}(\mathbf{n})\nu^{\mathbf{t}}(\mathbf{n}) &= \bar{f}^{\mathbf{t}}(\mathbf{N} - \mathbf{n})\bar{\mu}^{\mathbf{t}}(\mathbf{N} - \mathbf{n}) \end{aligned}$$

and hence $g^0 \odot \nu^0$ and $g^{\mathbf{t}} \odot \nu^{\mathbf{t}}$ produce the same diffraction patterns as $f^0 \odot \mu^0$ and $f^{\mathbf{t}} \odot \mu^{\mathbf{t}}$.

On the other hand, if $f^0 = [f_0^0, f_1^0]$ has a tight support in \mathcal{M}^0 , then (11)-(12) is an inconsistent construction of object estimate since $g^0 = [g_0^0, g_1^0]$ and $g^{\mathbf{t}} = [0, g_1^1]$ violate the overlap condition for $g_1^0 \neq 0$.

It is important to note that if just one part $f^{\mathbf{s}}$ has a tight support in $\mathcal{M}^{\mathbf{s}}$ and if the set of parts $\{f^{\mathbf{t}} : \mathbf{t} \in \mathcal{T}\}$ is strongly connected, then the ambiguities associated with loose support disappear with an overwhelming probability.

4. AMBIGUITIES IN THE MIXING SCHEMES

Once the loose support ambiguities are eliminated by using some support prior, the next ambiguities to tackle are those arising from poorly designed measurement schemes.

To proceed, we rewrite (5) as

$$(13) \quad \begin{aligned} h(\mathbf{n} + \mathbf{t}) &\equiv \ln g(\mathbf{n} + \mathbf{t}) - \ln f(\mathbf{n} + \mathbf{t}) \\ &= i\theta_{\mathbf{t}} - \ln \alpha(\mathbf{n}) - i\phi(\mathbf{n}) \pmod{i2\pi}, \quad \forall \mathbf{n} \in \mathcal{M}^0, \end{aligned}$$

whenever f and g are nonvanishing. For vanishing $g(\mathbf{n})$ and $f(\mathbf{n})$, including \mathbf{n} outside the object domain, $h(\mathbf{n})$ is not well-defined and can be set arbitrarily (and shall be set to maintain eq. (13)).

By (13) with $\mathbf{t} = (0, 0)$,

$$(14) \quad h(\mathbf{n}) = i\theta_0 - \ln \alpha(\mathbf{n}) - i\phi(\mathbf{n}), \quad \forall \mathbf{n} \in \mathcal{M}^0$$

and hence

$$(15) \quad h(\mathbf{n} + \mathbf{t}) - h(\mathbf{n}) = i\theta_{\mathbf{t}} - i\theta_0 \pmod{i2\pi}, \quad \forall \mathbf{t}, \mathbf{n}.$$

To this end, another theorem in [18] asserts that under (5), an affine phase factor and a constant amplitude offset are the only ambiguities for the *mixing schemes*.

First consider a simplest example of the mixing schemes.

Example 4.1. Consider a small perturbation to the raster-scan scheme with $\mathbf{t}_{10} = (\tau, 0)$, $\mathbf{t}_{20} = (2\tau - 1, 0)$, $\mathbf{t}_{01} = (0, \tau)$, $\mathbf{t}_{20} = (0, 2\tau - 1)$. Then

$$(16) \quad 2\mathbf{t}_{10} - \mathbf{t}_{20} = (1, 0), \quad h(\mathbf{n} + 2\mathbf{t}_{10} - \mathbf{t}_{20}) = h(\mathbf{n} + (1, 0))$$

$$(17) \quad 2\mathbf{t}_{01} - \mathbf{t}_{20} = (0, 1), \quad h(\mathbf{n} + 2\mathbf{t}_{01} - \mathbf{t}_{20}) = h(\mathbf{n} + (0, 1))$$

By (15)

$$\begin{aligned} h(\mathbf{n} + 2\mathbf{t}_{10} - \mathbf{t}_{20}) &= h(\mathbf{n} + 2\mathbf{t}_{10}) - i\theta_{20} + i\theta_{00}, \quad \forall \mathbf{n} \in (\mathcal{M}^0 - (a, 0)) \\ &= h(\mathbf{n} + \mathbf{t}_{10}) + i\theta_{10} - i\theta_{20}, \quad \forall \mathbf{n} \in (\mathcal{M}^0 - (a, 0)) \cap (\mathcal{M}^0 - \mathbf{t}_{10}) \\ &= h(\mathbf{n}) + 2i\theta_{10} - i\theta_{20} - i\theta_{00}, \quad \forall \mathbf{n} \in (\mathcal{M}^0 - (a, 0)) \cap (\mathcal{M}^0 - \mathbf{t}_{10}) \cap \mathcal{M}^0 \end{aligned}$$

as well as

$$\begin{aligned} h(\mathbf{n} + 2\mathbf{t}_{10} - \mathbf{t}_{20}) &= h(\mathbf{n} + \mathbf{t}_{10} - \mathbf{t}_{20}) + i\theta_{10} - i\theta_{00}, \quad \forall \mathbf{n} \in (\mathcal{M}^0 - (a, 0) + \mathbf{t}_{10}) \\ &= h(\mathbf{n} - \mathbf{t}_{20}) + 2i\theta_{10} - 2i\theta_{00}, \quad \forall \mathbf{n} \in (\mathcal{M}^0 - (a, 0) + \mathbf{t}_{10}) \cap (\mathcal{M}^0 - (a, 0) + 2\mathbf{t}_{10}) \\ &= h(\mathbf{n}) + 2i\theta_{10} - i\theta_{20} - i\theta_{00}, \quad \forall \mathbf{n} \in (\mathcal{M}^0 - (a, 0) + \mathbf{t}_{10}) \cap (\mathcal{M}^0 - (a, 0) + 2\mathbf{t}_{10}) \end{aligned}$$

modulo $i2\pi$. In other words,

$$(18) \quad h(\mathbf{n} + (1, 0)) = h(\mathbf{n}) + 2i\theta_{10} - i\theta_{20} - i\theta_{00}, \quad \pmod{i2\pi}, \quad \forall \mathbf{n} \in D$$

where

$$\begin{aligned} D &:= [\mathcal{M}^0 \cap (\mathcal{M}^0 - (1, 0)) \cap (\mathcal{M}^0 - \mathbf{t}_{10})] \cup [(\mathcal{M}^0 - (1, 0) + \mathbf{t}_{10}) \cap (\mathcal{M}^0 - (1, 0) + 2\mathbf{t}_{10})] \\ &= [\mathcal{M}^0 \cap (\mathcal{M}^0 - (1, 0)) \cap (\mathcal{M}^0 - (\tau, 0))] \cup [(\mathcal{M}^0 + (\tau - 1, 0)) \cap (\mathcal{M}^0 + (2\tau - 1, 0))]. \end{aligned}$$

We claim that (18) extends to all $\mathbf{n} \in \mathbb{Z}_n^2$.

Let $\llbracket k, l \rrbracket$ denote the integers between, and including, $k, l \in \mathbb{Z}$. First observe that

$$D = (\llbracket 0, m - \tau - 1 \rrbracket \cup \llbracket 2\tau - 1, m + \tau - 2 \rrbracket) \times \llbracket 0, m - 1 \rrbracket.$$

By (15) (with $\mathbf{t} = (\tau, 0)$), (18) for \mathbf{n} in the subset

$$\llbracket 0, m - \tau - 1 \rrbracket \times \llbracket 0, m - 1 \rrbracket \subset D$$

extends to

$$\llbracket \tau, m - 1 \rrbracket \times \llbracket 0, m - 1 \rrbracket$$

and hence to $\mathcal{M}^0 = \mathbb{Z}_m^2$. By (15), (18) extends to the object domain \mathbb{Z}_n^2 .

Similarly, from (17) it follows that

$$(19) \quad h(\mathbf{n} + (0, 1)) = h(\mathbf{n}) + 2i\theta_{01} - i\theta_{02} - i\theta_{00}, \quad \text{mod } i2\pi, \quad \forall \mathbf{n} \in \mathbb{Z}_n^2$$

and hence

$$(20) \quad h(\mathbf{n} + \mathbf{k}) = h(\mathbf{n}) + i\mathbf{k} \cdot \mathbf{r}, \quad \mathbf{n} \in \mathbb{Z}_n^2, \quad \mathbf{k} \in \mathbb{Z}^2$$

where

$$(21) \quad \mathbf{r} = \begin{bmatrix} 2(\theta_{10} - \theta_{00}) - (\theta_{20} - \theta_{00}) \\ 2(\theta_{01} - \theta_{00}) - (\theta_{02} - \theta_{00}) \end{bmatrix}.$$

Clearly, (18) and (19) determine $\alpha(\mathbf{n})$ and $\phi(\mathbf{n})$ for all $\mathbf{n} \in \mathcal{M}^0$ via

$$(22) \quad \begin{aligned} \alpha(\mathbf{n}) &= \alpha_0, \\ \phi(\mathbf{n} + (1, 0)) &= \phi(\mathbf{n}) + 2\theta_{10} - \theta_{20} - \theta_{00} \quad \text{mod } i2\pi, \quad \mathbf{n} \in \mathcal{M}^0, \end{aligned}$$

for some constant α_0 . Hence

$$(23) \quad \phi(\mathbf{n} + \mathbf{k}) - \phi(\mathbf{n}) = \mathbf{k} \cdot \mathbf{r}, \quad \text{mod } 2\pi,$$

Having shown that the probe phase error ϕ has an affine profile (23), let us now turn to the block phases θ_k .

By (13),

$$(24) \quad h(\mathbf{n} + \mathbf{t}_{kl}) = i\theta_{kl} - \ln \alpha_0 - i\phi(\mathbf{n}) \quad \text{mod } i2\pi, \quad \mathbf{n} \in \mathcal{M}^0, \quad \forall k, l = 0, \dots, q-1.$$

Substituting $\mathbf{n} = (0, 0)$ into (24) we have

$$h(\mathbf{t}_{kl}) = i\theta_{kl} - \ln \alpha_0 - i\phi(0) \quad \text{mod } i2\pi.$$

On the other hand, with the replacement $\mathbf{t}_{kl} \rightarrow \mathbf{t}_{00}$ and $\mathbf{n} \rightarrow \mathbf{t}_{kl}$ in (24), we have

$$h(\mathbf{t}_{kl}) = i\theta_{00} - \ln \alpha_0 - i\phi(\mathbf{t}_{kl}) \quad \text{mod } i2\pi$$

and hence

$$(25) \quad \theta_{kl} - \theta_0 = \phi(0) - \phi(\mathbf{t}_{kl}), \quad \forall k, l = 0, \dots, q-1.$$

It follows from (25) and (23) that

$$(26) \quad \theta_{kl} - \theta_0 + \mathbf{t}_{kl} \cdot \mathbf{r} = 0, \quad \text{mod } 2\pi, \quad \forall k, l = 0, \dots, q-1.$$

The above example is merely a special case of the general class of schemes satisfying the mixing property.

Slightly more sophisticated examples are randomly perturbed raster scans (2) and (1).

5. AMBIGUITIES IN RASTER-SCAN

The raster scan is well known to be a poorly designed measurement scheme. Periodic artifacts called the raster grid pathology are widely reported in the literature. To our knowledge, however, the raster grid pathology has not been systematically and precisely formulated.

5.1. **Phase drift.** Even though there are a lot more degrees in raster scan ambiguity, the block phase for raster scan is guaranteed to have an affine profile just as in the case of the mixing schemes [18]. But the corresponding ambiguity in object estimate takes a form different from the affine phase factor as Examples 5.1 and 5.2 show. Due to the constant stepping up of the phase in parts of the object in the direction of the scan, we refer the ambiguity as the *phase drift* ambiguity.

Example 5.1. Consider raster scan with the constant step $\mathbf{v} = (m/2, 0)$, 50% overlap between adjacent probes and periodic boundary condition. Partition the object and the probe with $q = 2n/m$ as

$$(27) \quad f = [f_0 \ f_1 \ \cdots \ f_{q-1}], \quad \mu^0 = [\mu_0 \ \mu_1]$$

and write the object and probe estimates as

$$(28) \quad g = [f_0 \ e^{i2\pi/q} f_1 \ \cdots \ e^{i2\pi(q-1)/q} f_{q-1}], \quad \nu^0 = [\mu_0 \ e^{-i2\pi/q} \mu_1]$$

where $f_j, g_j \in \mathbb{C}^{n \times m/2}$ and $\mu_i, \nu_i \in \mathbb{C}^{m \times m/2}$. It is easy to see that

$$(29) \quad \nu^k \odot g^k = e^{i2\pi k/q} \mu^k \odot f^k, \quad k = 0, \dots, q-1,$$

where f^k and g^k are the restrictions of f and g , respectively, to \mathcal{M}^k . For $q > 4$, the phase drift is sufficiently small for ν^0/μ^0 to satisfy the PPC with $\delta = 1/2$.

More generally, consider $\mathbf{v} = (\tau, 0)$ for $\tau = m/p, q = pn/m$ ($p = 2$ corresponds to the case above)

$$(30) \quad f = [f_0 \ f_1 \ \cdots \ f_{q-1}], \quad \mu^0 = [\mu_0 \ \mu_1 \ \cdots \ \mu_{p-1}]$$

$$(31) \quad g = [f_0 \ e^{i2\pi/q} f_1 \ \cdots \ e^{i2\pi(q-1)/q} f_{q-1}], \quad \nu^0 = [\mu_0 \ e^{-i2\pi/q} \mu_1 \ \cdots \ e^{-i2\pi(p-1)/q} \mu_{p-1}]$$

where $f_j, g_j \in \mathbb{C}^{n \times m/p}, \mu_i, \nu_i \in \mathbb{C}^{m \times m/p}$. For this scan pattern, the same relation (29) holds. For $q\delta > 2(p-1)$, ν^0/μ^0 satisfies the PPC with $\delta = 1/2$.

The following example is the 2D version of (27)-(28).

Example 5.2. For $q = 3, \tau = m/2$, let

$$(32) \quad f = \begin{bmatrix} f_{00} & f_{10} & f_{20} \\ f_{01} & f_{11} & f_{21} \\ f_{02} & f_{12} & f_{22} \end{bmatrix}, \quad g = \begin{bmatrix} f_{00} & e^{i2\pi/3} f_{10} & e^{i4\pi/3} f_{20} \\ e^{i2\pi/3} f_{01} & e^{i4\pi/3} f_{11} & f_{21} \\ e^{i4\pi/3} f_{02} & f_{12} & e^{i2\pi/3} f_{22} \end{bmatrix}$$

be the object and its reconstruction, respectively, where $f_{ij}, g_{ij} \in \mathbb{C}^{n/3 \times n/3}$. Let

$$(33) \quad \mu^{kl} = \begin{bmatrix} \mu_{00}^{kl} & \mu_{10}^{kl} \\ \mu_{01}^{kl} & \mu_{11}^{kl} \end{bmatrix}, \quad \nu^{kl} = \begin{bmatrix} \mu_{00}^{kl} & e^{-i2\pi/3} \mu_{10}^{kl} \\ e^{-i2\pi/3} \mu_{01}^{kl} & e^{-i4\pi/3} \mu_{11}^{kl} \end{bmatrix}, \quad k, l = 0, 1, 2,$$

be the probe and its estimate, respectively, where $\mu_{ij}^{kl}, \nu_{ij}^{kl} \in \mathbb{C}^{n/3 \times n/3}$.

It is verified straightforwardly that $\nu^{ij} \odot g^{ij} = e^{i(i+j)2\pi/3} \mu^{ij} \odot f^{ij}$.

5.2. Periodic ambiguity. Next we formulate the periodic, but otherwise arbitrary, ambiguity in raster scan. For a constant stepsize τ , the periodic ambiguity has τ^2 degree of freedom. In other words, the larger the stepsize, the greater the degrees of freedom in the periodic ambiguity. We break up the discussion into two cases: (i) the overlap percentage is greater than or equal to 50% ($\tau \leq m/1$); (ii) the overlap percentage is less than 50% ($\tau > m/2$).

Example 5.3. ($\tau \leq m/2$) The \mathbf{t}_{kl} -shifted probes μ^{kl} and ν^{kl} can be written as

$$\mu^{kl} = \begin{bmatrix} \mu_{00}^{kl} & \mu_{10}^{kl} & \cdots & \mu_{p-1,0}^{kl} \\ \mu_{01}^{kl} & \mu_{11}^{kl} & \cdots & \mu_{p-1,1}^{kl} \\ \vdots & \vdots & \vdots & \vdots \\ \mu_{0,p-1}^{kl} & \mu_{1,p-1}^{kl} & \cdots & \mu_{p-1,p-1}^{kl} \end{bmatrix}, \quad \nu^{kl} = \begin{bmatrix} \nu_{00}^{kl} & \nu_{10}^{kl} & \cdots & \nu_{p-1,0}^{kl} \\ \nu_{01}^{kl} & \nu_{11}^{kl} & \cdots & \nu_{p-1,1}^{kl} \\ \vdots & \vdots & \vdots & \vdots \\ \nu_{0,p-1}^{kl} & \nu_{1,p-1}^{kl} & \cdots & \nu_{p-1,p-1}^{kl} \end{bmatrix}$$

Let $\epsilon = [\alpha(\mathbf{n}) \exp(i\phi(\mathbf{n}))] \in \mathbb{C}^{\tau \times \tau}$, $\alpha(\mathbf{n}) \neq 0$, and $\nu_{ij}^{kl} = \epsilon \odot \mu_{ij}^{kl}$, $\forall k, l, i, j$. Consider the two objects

$$(34) \quad f = \begin{bmatrix} f_{00} & \cdots & f_{q-1,0} \\ \vdots & \vdots & \vdots \\ f_{0,q-1} & \cdots & f_{q-1,q-1} \end{bmatrix}, \quad g = \begin{bmatrix} g_{00} & \cdots & g_{q-1,0} \\ \vdots & \vdots & \vdots \\ g_{0,q-1} & \cdots & g_{q-1,q-1} \end{bmatrix}$$

with $f_{ij} = \epsilon \odot g_{ij}$. Clearly the two exit waves $\mu^{kl} \odot f^{kl}$ and $\nu^{kl} \odot g^{kl}$ are identical, up to a global factor and (5) is satisfied.

Example 5.4. ($\tau > m/2$) Let

$$\mu^{kl} = \begin{bmatrix} \mu_{00}^{kl} & \mu_{10}^{kl} & \mu_{20}^{kl} \\ \mu_{01}^{kl} & \mu_{11}^{kl} & \mu_{21}^{kl} \\ \mu_{02}^{kl} & \mu_{12}^{kl} & \mu_{22}^{kl} \end{bmatrix}, \quad \nu^{kl} = \begin{bmatrix} \nu_{00}^{kl} & \nu_{10}^{kl} & \nu_{20}^{kl} \\ \nu_{01}^{kl} & \nu_{11}^{kl} & \nu_{21}^{kl} \\ \nu_{02}^{kl} & \nu_{12}^{kl} & \nu_{22}^{kl} \end{bmatrix}$$

with

$$\begin{bmatrix} \nu_{00}^{kl} & \nu_{10}^{kl} \\ \nu_{01}^{kl} & \nu_{11}^{kl} \end{bmatrix} = \epsilon \odot \begin{bmatrix} \mu_{00}^{kl} & \mu_{10}^{kl} \\ \mu_{01}^{kl} & \mu_{11}^{kl} \end{bmatrix}$$

where $\epsilon = [\alpha(\mathbf{n}) \exp(i\phi(\mathbf{n}))] \in \mathbb{C}^{\tau \times \tau}$, $\alpha(\mathbf{n}) \neq 0$. Likewise, consider the two objects in (34) with

$$\begin{bmatrix} f_{3i,3j} & f_{3i+1,3j} \\ f_{3i,3j+1} & f_{3i+1,3j+1} \end{bmatrix} = \epsilon \odot \begin{bmatrix} g_{3i,3j} & g_{3i+1,3j} \\ g_{3i,3j+1} & g_{3i+1,3j+1} \end{bmatrix}, \quad i, j = 0, 1, 2, \dots$$

Again, the two exit waves $\mu^{kl} \odot f^{kl}$ and $\nu^{kl} \odot g^{kl}$ are identical, up to a global factor, and (5) is satisfied.

6. NUMERICAL RECONSTRUCTION

6.1. Test objects. Our first test image is 256-by-256 Cameraman+ i Barbara (CiB). The resulting test object has the phase range $\pi/2$. The second test object is Randomly-phased Phantom (RPP) defined by $f_* = P \odot e^{i\phi}$ where P is the standard phantom (Fig. 3(a)) and $\{\phi(\mathbf{n})\}$ are i.i.d. uniform random variables over $[0, 2\pi]$. RPP has the maximal phase range because of its noise-like phase profile. In addition to the huge phase range, RPP has loosely supported parts with respect to the measurement schemes (see below) due to its thick dark

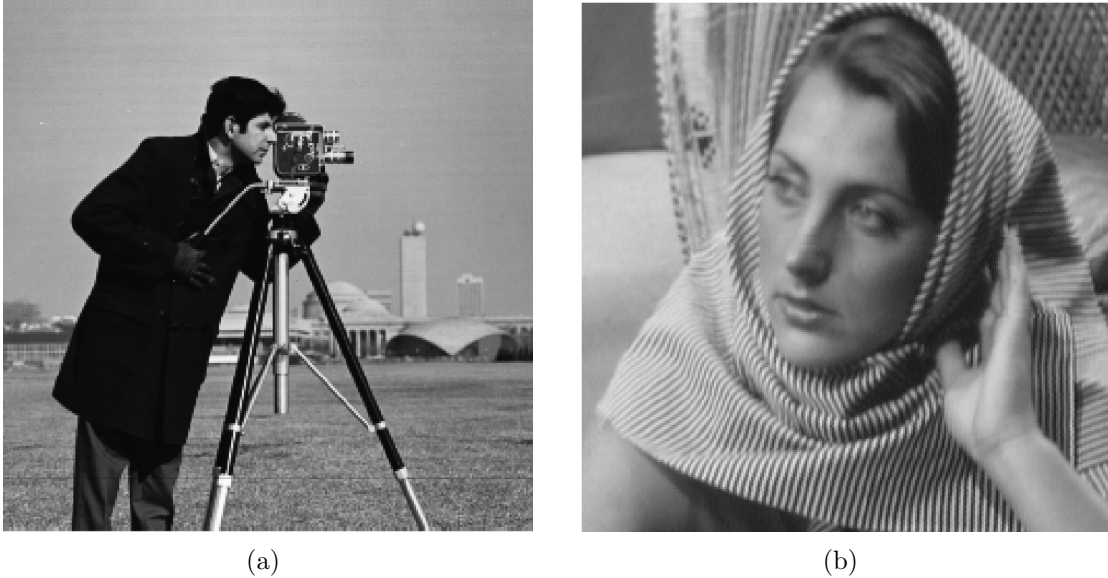


FIGURE 2. (a) The real part and (b) the imaginary part of the first test image.

margins around the oval. The third test object is the salted RPP, the sum of RPP and the salt noise (Fig. 3 (c)(d)). The salted noise is i.i.d, binomial random variables with probability 0.02 to be a complex constant in the form of $a(1+i)$, $a \in \mathbb{R}$, and probability 0.98 to be zero. The salt noise reduces the support looseness without significantly changing the original image and makes the salted RPP strongly connected in the sense (6). We explore the potential of adding salt for enhancing ptychographic reconstruction. The added salt can be removed in postprocessing by denoising after the salted version is well reconstructed.

6.2. Random probes. The probe size is 60×60 . In addition to the i.i.d. probe, we consider also correlated probe produced by convolving the i.i.d. probe with characteristic function of the set $\{(k_1, k_2) \in \mathbb{Z}^2 : \max\{|k_1|, |k_2|\} \leq c \cdot m; c \in (0, 1]\}$ where the constant c is a measure of the correlation length in the unit of $m = 60$ (Fig. 4).

6.3. Scanning schemes. We test two measurement schemes. The first is

$$\text{Rank-one perturbation} \quad \mathbf{t}_{kl} = \tau(k, l) + (\delta_k^1, \delta_l^2)$$

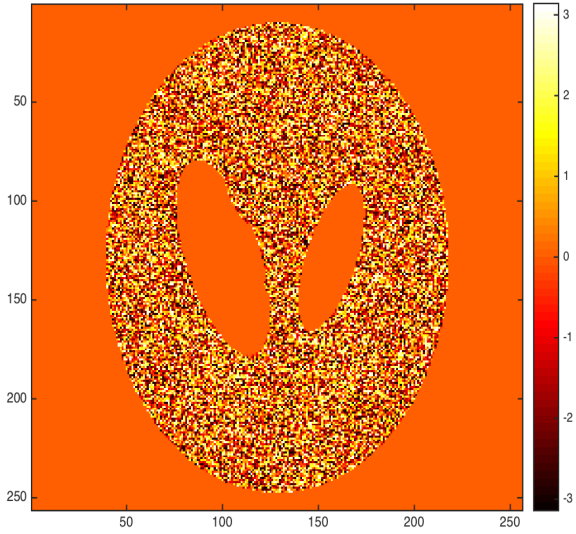
where δ_k^1 and δ_l^2 are i.i.d. uniform random variables over $[-4, 4]$. The second is

$$\text{Full-rank perturbation} \quad \mathbf{t}_{kl} = \tau(k, l) + (\delta_{kl}^1, \delta_{kl}^2)$$

with the reference stepsize $\tau = 30$ where δ_{kl}^1 and δ_{kl}^2 are i.i.d. uniform random variables over $[-4, 4]$. In other words, the adjacent probes overlap by roughly $\tau/m = 50\%$. In experiments reported in the literature the adjacent illuminated areas typically have an overlap 60-70% [8, 39].



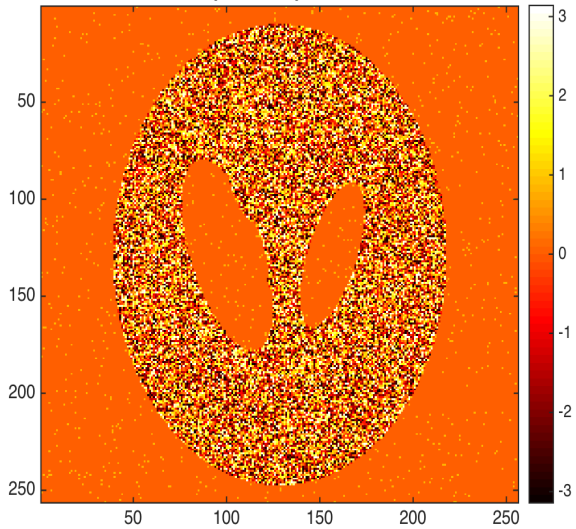
(a) The phantom



(b) The phase



(c) The salted phantom



(d) The salted phase

FIGURE 3. (a) phantom, (b) the phase of RPP, (c) salted phantom and (d) the phase of the salted RPP.

6.4. Alternating minimization. Let $A^*(\nu, g)$ be the ptychographic measurement data with the mask ν and the object g . Set $A_k^*g := A^*(\mu_k, g)$, $k \geq 1$, with the k -th probe estimate μ_k and $B_k^*\nu := A^*(\nu, f_{k+1})$, $k \geq 1$, with the $(k+1)$ -st image estimate f_{k+1} such that $A_k^*f_{j+1} = B_j^*\mu_k$, $j \geq 1, k \geq 1$.

A main feature of alternating minimization scheme is the monotonicity property:

$$\mathcal{L}(A_k^*f_k) \geq \mathcal{L}(A_{k+1}^*f_{k+1}), \quad \mathcal{L}(B_k^*\mu_k) \geq \mathcal{L}(B_{k+1}^*\mu_{k+1}).$$

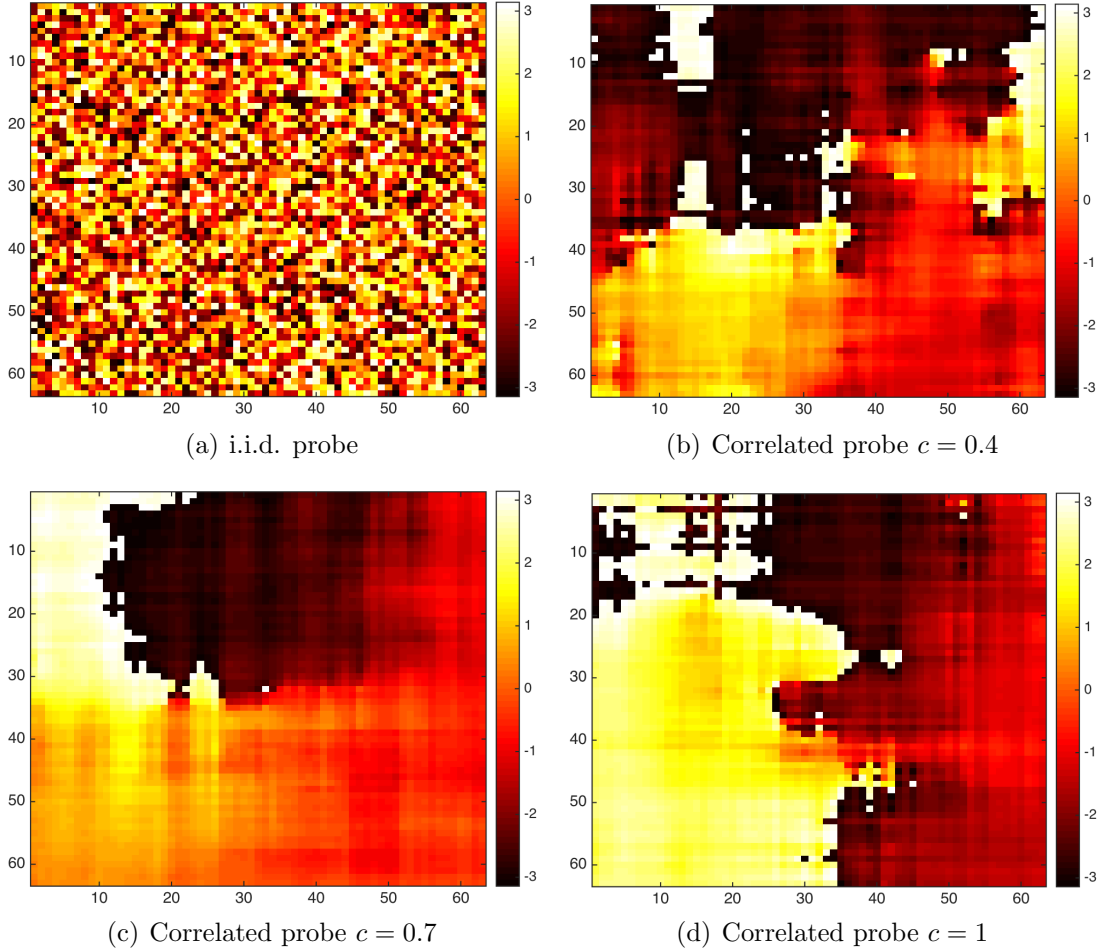


FIGURE 4. The phase profile of (a) the i.i.d. probe and (b)(c)(d) the correlated probes of various correlation lengths.

Algorithm 1: Alternating minimization (AM)

- 1: Input: initial probe guess $\mu_1 \in \text{PPC}(\mathbf{k}, \delta)$.
 - 2: Update the object estimate $f_{k+1} = \arg \min \mathcal{L}(A_k^* g)$ s.t. $g \in \mathbb{C}^{n^2}$.
 - 3: Update the probe estimate $\mu_{k+1} = \arg \min \mathcal{L}(B_k^* \nu)$ s.t. $\nu \in \mathbb{C}^{m^2}$.
 - 4: Terminate if $\| |B_k^* \mu_{k+1}| - b \|_2$ stagnates or is less than tolerance; otherwise, go back to step 2 with $k \rightarrow k + 1$.
-

We consider two log-likelihood cost functions [6, 59] for noise-robustness

$$(35) \quad \text{Poisson: } \mathcal{L}(y) = \sum_i |y[i]|^2 - b^2[i] \ln |y[i]|^2$$

$$(36) \quad \text{Gaussian: } \mathcal{L}(y) = \frac{1}{2} \| |y| - b \|_2^2$$

based on the maximum likelihood principle for the Poisson noise model. The Poisson log-likelihood function (35) is asymptotically reduced to the (36) as shown in Appendix A.

The ptychographic iterative engines, PIE [52], ePIE [39] and r-PIE [37], are both derived from the amplitude-based cost function (36). The maximum likelihood scheme is also a variance stabilization scheme which uniformizes the probability distribution for every pixel regardless of the measured intensity value [33]. It is well established that the amplitude-based cost function (36) outperforms the intensity-based cost function $\frac{1}{2}\| |y|^2 - b^2 \|_2^2$ [63]. See [23, 67] for more choices of objective functions.

For non-convex iterative optimization, a good initial guess or some regularization is usually crucial for convergence [6, 59]. A novelty of our approach is to base the initial guess for the probe on PPC. To test the linear phase ambiguity, we consider the probe initialization

$$(37) \quad \mu_1(\mathbf{n}) = \mu^0(\mathbf{n}) \exp \left[i2\pi \frac{\mathbf{k} \cdot \mathbf{n}}{n} \right] \exp [i\phi(\mathbf{n})], \quad \mathbf{n} \in \mathcal{M}^0$$

where $\phi(\mathbf{n})$ are independently and uniformly distributed on $(-\delta\pi, \delta\pi)$. We use $\delta \in [0, 1/2]$ as the control parameter for the proximity of the initial probe to the true probe, modulo a linear phase factor represented by \mathbf{k} , and denote this class of probe initialization by PPC(\mathbf{k}, δ).

To simplify the algorithm, we do not enforce PPC in subsequent iterations. Note also that according to (22), it is unnecessary in theory to impose the phase probe constraint $|\mu(\mathbf{k})| = 1$ in step 3. In practice, however, imposing the phase probe constraint does speed up the convergence (see below for how the phase probe constraint is enforced).

6.5. DR splitting (DRS). The inner loops of AM are computed by the Douglas-Rachford splitting (DRS) method which is a proximal point algorithm for minimizing the sum of two objective functions

$$(38) \quad \min_u F(u) + \mathcal{L}(u).$$

The DR splitting method is defined by the following iteration for $l = 1, 2, 3 \dots$

$$(39) \quad \begin{aligned} y^{l+1} &= \text{prox}_{F/\rho}(u^l); \\ z^{l+1} &= \text{prox}_{\mathcal{L}/\rho}(2y^{l+1} - u^l) \\ u^{l+1} &= u^l + z^{l+1} - y^{l+1} \end{aligned}$$

where $\text{prox}_{\mathcal{L}/\rho}(u^k) := \underset{x}{\text{argmin}} \mathcal{L}(x) + \frac{\rho}{2}\|x - u^k\|^2$. For the initial guess u_1^1 in our simulations, we let $u_1^1 = A_1^* f_1$ where $f_1(\mathbf{n})$ is a phase object with i.i.d. phase uniformly distributed over $[0, 2\pi]$ or a constant value 0.

Since we demand that the minimum of (38) corresponds to the solution of the ptychographic phase retrieval with the assumed probe estimate μ_k in the k -th epoch, we let $F(u)$ be the indicator function $\chi_k(u)$ of the range of A_k^* , i.e. $\chi_k(u) = 0$ if y is in the range of A_k^* ; and $\chi_k(u) = \infty$ otherwise. For this choice of F , $\text{prox}_{F/\rho}(u) = A_k^*(A_k^*)^\dagger u$ is independent of ρ .

For any $y \in \mathbb{C}^{m^2}$, $\text{sgn}(y)$ is defined as

$$\text{sgn}(y)[j] = \begin{cases} 1 & \text{if } y[j] = 0 \\ y[j]/|y[j]| & \text{else.} \end{cases}$$

For the Gaussian case, the object estimate is updated by

$$(40) \quad f_{k+1} = (A_k^*)^\dagger u_k^{l+1}$$

after the termination of the following iteration

$$(41) \quad y_k^l = A_k^* (A_k^*)^\dagger u_k^l$$

$$(42) \quad z_k^l = \frac{1}{\rho+1} b \odot \text{sgn}(2y_k^l - u_k^l) + \frac{\rho}{\rho+1} (2y_k^l - u_k^l)$$

$$(43) \quad u_k^{l+1} = u_k^l + z_k^l - y_k^l$$

which can be summarized compactly as

$$(44) \quad u_k^{l+1} = \frac{1}{\rho+1} u_k^l + \frac{\rho-1}{\rho+1} A_k^* (A_k^*)^\dagger u_k^l + \frac{1}{\rho+1} b \odot \text{sgn}(2A_k^* (A_k^*)^\dagger u_k^l - u_k^l).$$

Likewise, with the phase probe constraint, the probe is updated by

$$(45) \quad \mu_{k+1} = \text{sgn}((B_k^*)^\dagger v_k^{l+1})$$

where v_k^{l+1} is the terminal output of the following iteration

$$(46) \quad v_k^{l+1} = \frac{1}{\rho+1} v_k^l + \frac{\rho-1}{\rho+1} B_k^* \text{sgn}((B_k^*)^\dagger v_k^l) + \frac{1}{\rho+1} b \odot \text{sgn}(2B_k^* \text{sgn}((B_k^*)^\dagger v_k^l) - v_k^l).$$

For the Poisson case, the inner loops become

$$(47) \quad \begin{aligned} \bar{u}_k^{l+1} &= \frac{\rho+4}{2\rho+4} u_k^l - \frac{2}{2+\rho} A_k^* (A_k^*)^\dagger u_k^l + \\ &\quad \frac{\rho}{2\rho+4} \sqrt{|2A_k^* (A_k^*)^\dagger u_k^l - u_k^l|^2 + \frac{8(2+\rho)}{\rho^2} b^2 \odot \text{sgn}(2A_k^* (A_k^*)^\dagger u_k^l - u_k^l)} \end{aligned}$$

$$(48) \quad \begin{aligned} \bar{v}_k^{l+1} &= \frac{\rho+4}{2\rho+4} v_k^l - \frac{2}{\rho+2} B_k^* \text{sgn}((B_k^*)^\dagger v_k^l) + \\ &\quad \frac{\rho}{2\rho+4} \sqrt{|2B_k^* \text{sgn}((B_k^*)^\dagger v_k^l) - v_k^l|^2 + \frac{8(2+\rho)}{\rho^2} b^2 \odot \text{sgn}(2B_k^* \text{sgn}((B_k^*)^\dagger v_k^l) - v_k^l)}. \end{aligned}$$

After the inner loops terminate, the object and probe are updated as (40) and (45), respectively.

The pseudoinverses $(A_k^*)^\dagger = (A_k A_k^*)^{-1} A_k$ and $(B_k^*)^\dagger = (B_k B_k^*)^{-1} B_k$ are easy to compute since $A_k A_k^*$ and $B_k B_k^*$ are diagonal.

We shall refer to the Douglas-Rachford Splitting method with the Poisson log-likelihood function and the Gaussian version by the acronyms *Poisson-DRS* and *Gaussian-DRS*, respectively. We call the above algorithms as Alternating Minimization with Douglas-Rachford Splitting (AMDRS).

We fix the DRS parameter $\rho = 1$ in all simulations. As a result, (44)-(46) become

$$(49) \quad u_k^{l+1} = \frac{1}{2} u_k^l + \frac{1}{2} b \odot \text{sgn}(2A_k^* (A_k^*)^\dagger u_k^l - u_k^l)$$

$$(50) \quad v_k^{l+1} = \frac{1}{2} v_k^l + \frac{1}{2} b \odot \text{sgn}(2B_k^* \text{sgn}((B_k^*)^\dagger v_k^l) - v_k^l).$$

and (47)-(48) become

$$(51) \quad u_k^{l+1} = \frac{5}{6}u_k^l - \frac{2}{3}A_k^*(A_k^*)^\dagger u_k^l + \frac{1}{6}\sqrt{|2A_k^*(A_k^*)^\dagger u_k^l - u_k^l|^2 + 24b^2} \odot \text{sgn}\left(2A_k^*(A_k^*)^\dagger u_k^l - u_k^l\right)$$

$$(52) \quad v_k^{l+1} = \frac{5}{6}v_k^l - \frac{2}{3}B_k^*\text{sgn}\left((B_k^*)^\dagger v_k^l\right) + \frac{1}{6}\sqrt{|2B_k^*\text{sgn}\left((B_k^*)^\dagger v_k^l\right) - v_k^l|^2 + 24b^2} \odot \text{sgn}\left(2B_k^*\text{sgn}\left((B_k^*)^\dagger v_k^l\right) - v_k^l\right).$$

6.6. Error metrics. We use relative error (RE) and relative residual (RR) as the merit metrics for the recovered image f_k and probe μ_k at the k^{th} epoch:

$$(53) \quad \text{RE}(k) = \min_{\alpha \in \mathbb{C}, \mathbf{k} \in \mathbb{R}^2} \frac{\|f(\mathbf{k}) - \alpha e^{-i2\pi\mathbf{k}\cdot\mathbf{r}/n} f_k(\mathbf{k})\|_2}{\|f\|_2}$$

$$(54) \quad \text{RR}(k) = \frac{\|b - |A_k^* f_k|\|_2}{\|b\|_2}.$$

Note that in (53) the linear phase ambiguity is discounted along with a complex scaling factor. When we want to demonstrate the effectiveness of certain techniques in removing the linear phase ambiguity, we resort to a different error metric

$$(55) \quad \text{RE2}(k) = \min_{\alpha \in \mathbb{C}} \frac{\|f(\mathbf{k}) - \alpha f_k(\mathbf{k})\|_2}{\|f\|_2}$$

6.7. Boundary conditions. The ptychographic measurements when the probe steps outside of the boundary of the object domain need special treatment in the reconstruction process.

The periodic boundary condition conveniently treats all diffraction patterns and object pixels in the same way. The bright-field boundary condition assumes known, nonzero values for the pixels outside of the object domain and has the capability of removing the linear phase ambiguity from the object estimate. However, its rate of convergence and accuracy of reconstruction depends on the contrast between the boundary value and the object values. The larger the contrast, the greater the basin of attraction and the faster the convergence for the iteration. On the contrary, the dark-field boundary condition assumes the zero value for the pixels outside of the object domain but can not remove the linear phase ambiguity. As a result, the limit of vanishing bright-field boundary condition is a singular one.

6.8. Different combinations. First we compare performance of AMDRS with different combinations of objective functions, scanning schemes and random probes in the case of noiseless measurements with the periodic boundary condition. We use the stopping criteria for the inner loops:

$$\frac{\||A_k^*(A_k^*)^\dagger u_k^l| - b\|_2 - \||A_k^*(A_k^*)^\dagger u_k^{l+1}| - b\|_2}{\||A_k^*(A_k^*)^\dagger u_k^l| - b\|_2} \leq 10^{-4}$$

with the maximum number of iterations capped at 60.

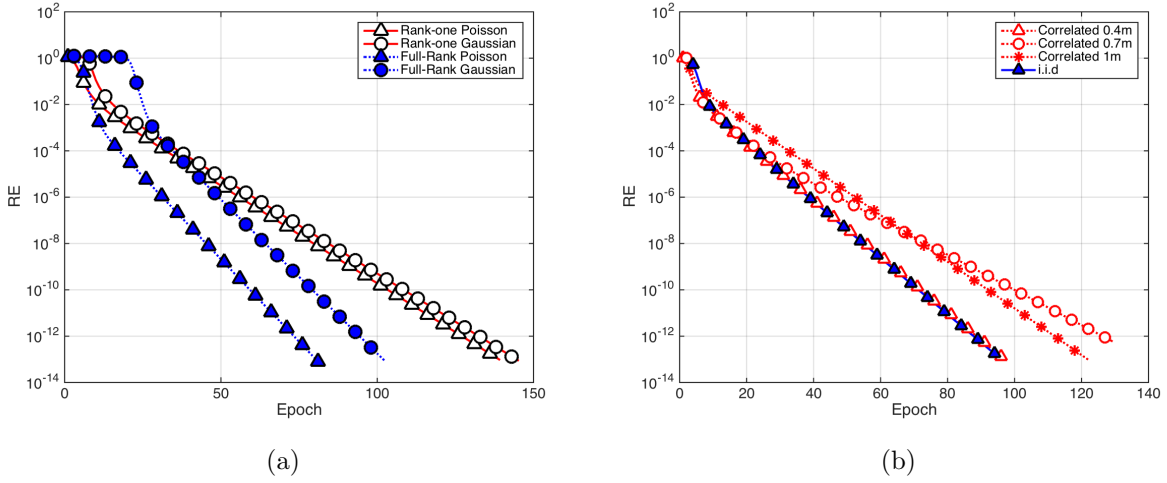


FIGURE 5. Geometric convergence to CiB at various rates for (a) Four combinations of objective functions and scanning schemes with i.i.d. probe (rank-one Poisson, $r_o = 0.8236$; rank-one Gaussian, $r_o = 0.8258$; full-rank Poisson, $r_o = 0.7205$; full-rank Gaussian, $r_o = 0.7373$) and (b) Poisson-DRS with four probes of different correlation lengths ($r_o = 0.7583$ for $c = 0.4$; $r_o = 0.8394$ for $c = 0.7$; $r_o = 0.7932$ for $c = 1$; $r_o = 0.7562$ for iid probe)

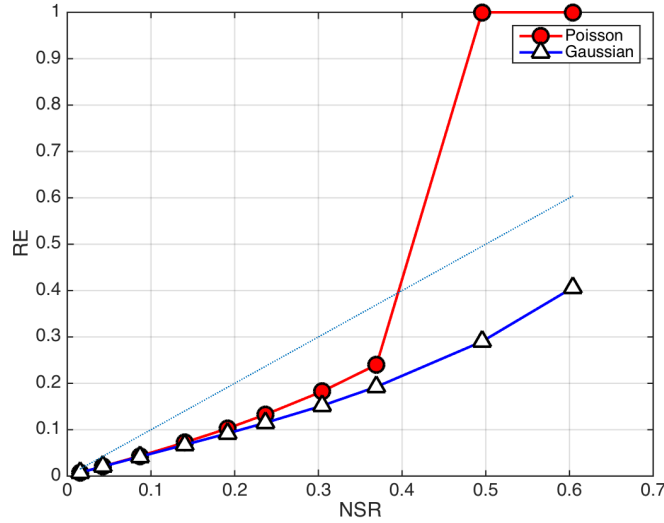


FIGURE 6. RE versus NSR

Figure 5 shows geometric convergence of RE (53) at various rates of convergence r_o to the test object CiB. In particular, Fig. 5(a) shows that the full-rank scheme outperforms the rank-one scheme and that Poisson-DRS outperforms (slightly) Gaussian-DRS while Figure 5(b) shows that the i.i.d. probe yields the smallest rate of convergence ($r_o = 0.7562$) closely followed by the rate ($r_o = 0.7583$) for $c = 0.4$.

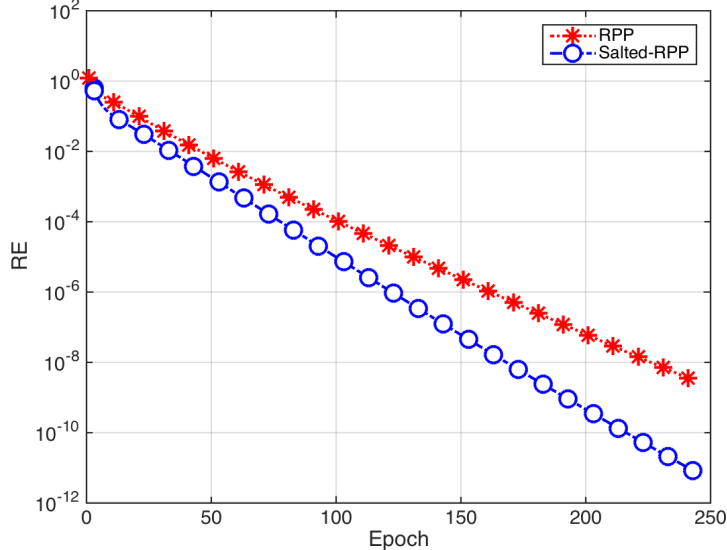


FIGURE 7. Adding salt noise speeds up the convergence.

6.9. **Poisson noise.** For noisy measurement, the size of the noise is measured in terms of the noise-to-signal ratio (NSR).

$$\text{NSR} = \frac{\|b - |A_0^* f_0\|_2}{\|A_0^* f_0\|_2}$$

Figure 6 shows REs versus NSR for Poisson-DRS and Gaussian-DRS with the periodic boundary condition, i.i.d. probe and the full-rank scheme. The maximum number of epoch is limited to 100. The RR stabilizes usually after 30 epochs. The (blue) reference straight line has slope 1. We see that the Gaussian-DRS outperforms the Poisson-DRS, especially when the Poisson RE becomes unstable for $\text{NSR} \geq 35\%$. As noted in [11, 37, 69] fast convergence (with the Poisson log-likelihood function) may introduce noisy artifacts and reduce reconstruction quality.

For the rest of the experiments, we use noiseless data, Poisson-DRS and the full-rank scheme.

6.10. **Dark pixels.** Extensive area of dark pixels can pose a challenge to ptychographic reconstruction. As shown in Fig. 7, the rate ($r_o = 0.9345$) of convergence for RPP is larger than that for CiB in Fig. 5. Adding salt to RPP can speed up the convergence slightly, resulting in a smaller rate of 0.9115. Fig. 7 and 8 show the phase error of the reconstruction for RPP and salted RPP, respectively.

Another effect of the dark margin in RPP is that \mathbf{r} of the linear phase ambiguity may be non-integers since the periodic boundary condition is ineffective on the dark margin. Adding salts can force \mathbf{r} to be integers. For example, $\mathbf{r} = (0, -1.231)$ for RPP while $\mathbf{r} = (-1, -1)$ for the salted RPP in Fig. 7 and 8.

As mentioned above, the linear phase ambiguity always accompanies ptychographic reconstruction with either the periodic or dark-field (boundary value = 0) boundary condition.

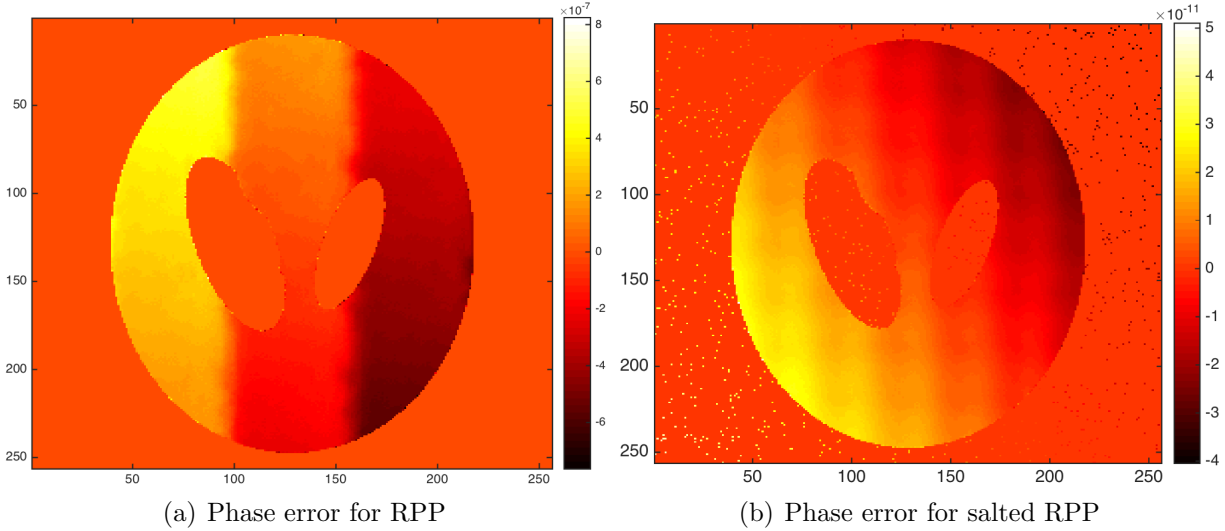


FIGURE 8. Phase difference between the true object and the reconstruction. Note the different scales in (b) and (c).

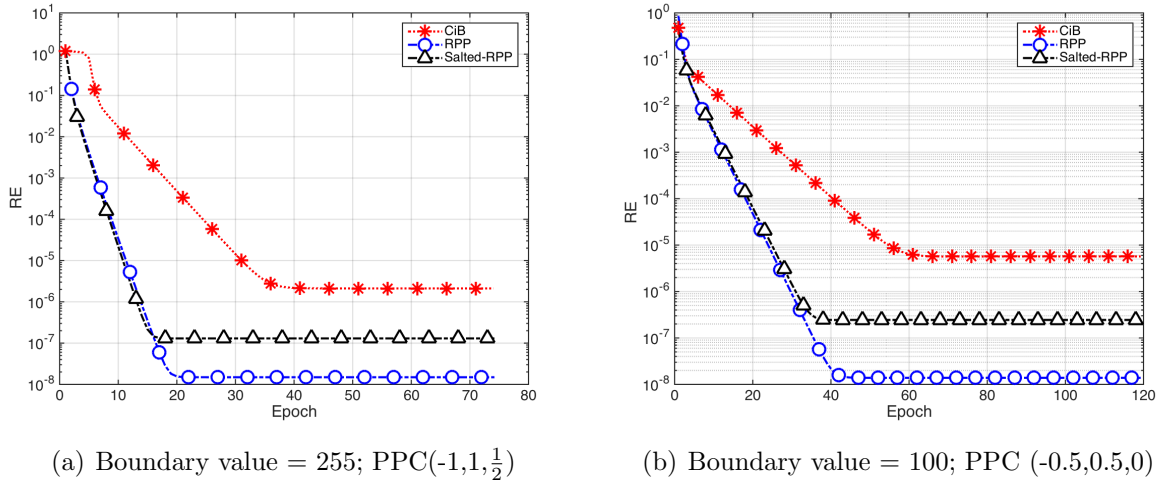


FIGURE 9. Oversample CiB, RPP, Salted RPP, DRAM diff-intensity

Next we demonstrate that the linear phase ambiguity is absent with the bright-field boundary condition.

6.11. Bright-field boundary condition. For the bright-field boundary condition, we set $f(\mathbf{n}) = c_0 \neq 0$ for $\mathbf{n} \in \mathbb{Z}_n^2$ where $c_0 \in \mathbb{C}$ is known.

We use the more stringent stopping rule

$$\frac{\| |A_k^*(A_k^*)^\dagger u_k^l | - b \|_2 - \| |A_k^*(A_k^*)^\dagger u_k^{l+1} | - b \|_2}{\| |A_k^*(A_k^*)^\dagger u_k^l | - b \|_2} \leq 10^{-5}$$

with the maximum number of iteration capped at 80.

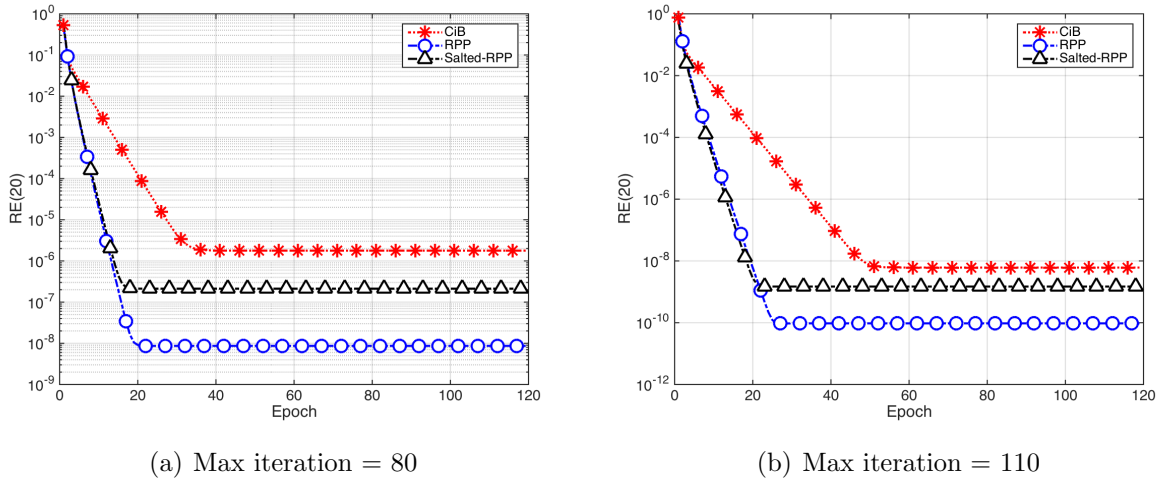


FIGURE 10. Boundary value = 255; PPC(-0.5, 0.5, 0)

Fig. 9 and 10 demonstrate the capability of the bright-field boundary condition to eliminate the linear phase ambiguity as the stronger error metric (55) decays geometrically before settling down to the final level of accuracy. The higher boundary value ($c_0 = 255$ in Fig. 9(a)) leads to faster convergence than the lower boundary value ($c_0 = 100$ in Fig. 9(b)). The final accuracy of reconstruction, however, depends on how accurately the inner loops for each epoch are solved. For example, increasing the maximum number of iteration from 80 to 110, significantly enhances the final accuracy of reconstruction (Fig. 10).

7. CONCLUSION

In the present work, we have presented concrete examples to illustrate theory of uniqueness in blind ptychography where both the object and the probe are simultaneously sought. Two opposing classes of measurement schemes are discussed: the mixing schemes and the raster scans. The former generally admit only a complex scaling factor and a linear phase ambiguity as ambiguities while the latter a host of other ambiguities of many degrees of freedom.

We have also presented a reconstruction algorithm AMDRS based on alternating minimization by Douglas-Rachford splitting. Enabled by an initialization method informed by the probe phase constraint in the theory of uniqueness, AMDRS converges globally and geometrically in all our experiments. Further, we have introduced the technique of bright-field boundary condition to remove the linear phase ambiguity and accelerate convergence, and the technique of adding salt noise to improve the quality of reconstruction of objects exhibiting extensive area of dark pixels.

APPENDIX A. THE POISSON VERSUS GAUSSIAN LOG-LIKELIHOOD FUNCTIONS

Poisson distribution

$$P_n = \frac{\lambda^n e^{-\lambda}}{n!}$$

Let $z = n = \lambda(1 + \epsilon)$ where $\lambda \gg 1$ and $\epsilon \ll 1$. Using Stirling's formula

$$z! \sim \sqrt{2\pi z} e^{-z} z^z$$

in the Poisson distribution, we obtain

$$\begin{aligned} P_n &\sim \frac{\lambda^{\lambda(1+\epsilon)} e^{-\lambda}}{\sqrt{2\pi} e^{-\lambda(1+\epsilon)} [\lambda(1+\epsilon)]^{\lambda(1+\epsilon)+1/2}} \\ &\sim \frac{1}{\sqrt{2\pi\lambda} e^{-\lambda\epsilon} (1+\epsilon)^{\lambda(1+\epsilon)+1/2}}. \end{aligned}$$

By the asymptotic

$$(1 + \epsilon)^{\lambda(1+\epsilon)+1/2} \sim e^{\lambda\epsilon + \lambda\epsilon^2/2}$$

we have

$$P_n \sim \frac{e^{-\lambda\epsilon^2/2}}{\sqrt{2\pi\lambda}} = \frac{e^{-(z-\lambda)^2/(2\lambda)}}{\sqrt{2\pi\lambda}}.$$

The term $z - \lambda$ implies the Gaussian noise should be added to $|y_0|^2$ (not $|y_0|$) and the noise is independent but not identically distributed from pixel to pixel. More precisely, the variance of the noise should be proportional to the intensity of the diffraction pattern, i.e.

$$\lambda\epsilon = \xi\sqrt{\lambda},$$

where $\xi \sim N(0, 1)$. The overall SNR can be tuned by varying the total energy $\|y_0\|^2$.

The log-likelihood function becomes

$$(56) \quad \sum_j \ln |y[j]| + \frac{1}{2} \left| \frac{b[j]}{|y[j]|} - |y[j]| \right|^2, \quad b = \text{noisy diffraction pattern}.$$

The first approximation is the case of small noise, $\sqrt{b[j]} \approx |y_0[j]|$, and good initial point $\sqrt{b[j]} \approx |y[j]|$. After the substitution

$$\frac{\sqrt{b[j]}}{|y[j]|} \rightarrow 1, \quad \ln |y[j]| \rightarrow \ln \sqrt{b[j]}$$

the log-likelihood function becomes

$$(57) \quad \frac{1}{2} \sum_j \left| \sqrt{b[j]} - |y[j]| \right|^2, \quad b = \text{noisy diffraction pattern}.$$

Acknowledgements. The research of A. F. is supported by the US National Science Foundation grant DMS-1413373. AF thanks National Center for Theoretical Sciences (NCTS), Taiwan, where the present work was carried out, for the hospitality during his visits in June and August 2018.

REFERENCES

- [1] B. Abbey, K. A. Nugent, G. J. Williams, J.N. Clark, A.G. Peele, M.A. Pfeiffer, M. De Jonge & I. McNulty, “Keyhole coherent diffractive imaging.” *Nat. Phys.* **4** (2008) 394-398.
- [2] P. F. Almero and S. G. Hanson, “Random phase plate for wavefront sensing via phase retrieval and a volume speckle field,” *Appl. Opt.* **47** 2979-2987 (2008).
- [3] P. F. Almero, G. Pedrini, P. N. Gundu, W. Osten, S. G. Hanson, “Enhanced wavefront reconstruction by random phase modulation with a phase diffuser,” *Opt. Laser Eng.* **49** 252-257 (2011).
- [4] R. H. T. Bates, “Fourier phase problems are uniquely solvable in more than one dimension. 1. Underlying theory.”, *Optik* **61(3)** (1982): 247-262.
- [5] Yu. M. Bruck and L. G. Sodin, “On the ambiguity of the image reconstruction problem,” *Opt. Commun.***30**, 304-308 (1979).
- [6] L. Bian, J. Suo, J. Chung, X. Ou, C. Yang, F. Chen, and Q. Dai, “Fourier ptychographic reconstruction using Poisson maximum likelihood and truncated Wirtinger gradient,” *Sci. Rep.* **6**, 27384 (2016).
- [7] R. Bräuer, U. Wojak, F. Wyrowski, O. Bryngdahl, “Digital diffusers for optical holography,” *Opt. Lett.* **16**, 14279 (1991).
- [8] O. Bunk, M. Dierolf, S. Kynde, I. Johnson, O. Marti, F. Pfeiffer, “Influence of the overlap parameter on the convergence of the ptychographical iterative engine,” *Ultramicroscopy* **108** (5) (2008) 481-487.
- [9] H.N. Chapman & K.A. Nugent, “Coherent lensless X-ray imaging,” *Nat. Photon.* **4** (2010) 833-839.
- [10] P. Chen and A. Fannjiang, “Coded-aperture ptychography: uniqueness and reconstruction”, *Inverse Problems* **34** (2018) 025003.
- [11] P. Chen, A. Fannjiang and G. Liu, “Phase retrieval with one or two coded diffraction patterns by alternating projection with the null initialization,” *J. Fourier Anal. Appl.* 2017, DOI 10.1007/s00041-017-9536-8.
- [12] J.C. Silva and A. Menzel, “Elementary signals in ptychography,” *Opt. Exp.* **23** (2015) 33812-33821.
- [13] H.H. Conway & N.J.A. Sloane, *Sphere Packings, Lattices and Groups*, 3rd ed., Berlin, New York: Springer-Verlag, 1999.
- [14] M. Dierolf, A. Menzel, P. Thibault, P. Schneider, C. M. Kewish, R. Wepf, O. Bunk, and F. Pfeiffer, “Ptychographic x-ray computed tomography at the nanoscale,” *Nature* **467** (2010), 436-439.
- [15] M. Dierolf, P. Thibault, A. Menzel, C. Kewish, K. Jefimovs, I. Schlichting, K. Kong, O. Bunk, and F. Pfeiffer, “Ptychographic coherent diffractive imaging of weakly scattering specimens,” *New J. Phys.* **12** (2010), 035017.
- [16] R. Egami, R. Horisaki, L. Tian & J. Tanida, “Relaxation of mask design for single-shot phase imaging with a coded aperture,” *Appl. Opt.* **55** (2016) 1830-1837.
- [17] A. Fannjiang, “Absolute uniqueness of phase retrieval with random illumination,” *Inverse Problems* **28** (2012), 075008 (2012).
- [18] A. Fannjiang & P. Chen, “Blind ptychography: uniqueness and ambiguities”, preprint 2018.
- [19] A. Fannjiang and W. Liao, “Fourier phasing with phase-uncertain mask,” *Inverse Problems* **29** (2013) 125001.
- [20] H.M.L. Faulkner and J.M. Rodenburg, “Movable aperture lensless transmission microscopy: A novel phase retrieval algorithm,” *Phys. Rev. Lett.***93:2** (2004), 023903.
- [21] H.M.L. Faulkner and J.M. Rodenburg, “Error tolerance of an iterative phase retrieval algorithm for moveable illumination microscopy,” *Ultramicroscopy* **103:2** (2005), 153-164.
- [22] S. Gao, P. Wang, F. Zhang, G. T. Martinez, P. D. Nellist, X. Pan & A. I. Kirkland, “Electron ptychographic microscopy for three-dimensional imaging,” *Nat. Comm.* **18** 163 (2017)
- [23] P. Godard, M. Allain, V. Chamard, and J. Rodenburg, “Noise models for low counting rate coherent diffraction imaging,” *Opt. Express* **20**, 25914-25934 (2012).
- [24] M. Guizar-Sicairos, J.R. & Fienup, “Phase retrieval with transverse translation diversity: a nonlinear optimization approach.” *Opt. Express* **16** (2008), 7264-7278.
- [25] M. Hayes, “The reconstruction of a multidimensional sequence from the phase or magnitude of its Fourier transform,” *IEEE Trans. Acoust. Speech Signal Process.* **30** (1982), 140-154.

- [26] W. Hoppe, “Beugung im inhomogenen Primrstrahlwellenfeld. I. Prinzip einer Phasenmessung von Elektronenbeugungsinterferenzen”. *Acta Cryst. A* **25** (4) (1969) 495.
- [27] W. Hoppe, “Beugung im inhomogenen Primrstrahlwellenfeld. III. Amplituden- und Phasenbestimmung bei unperiodischen Objekten”, *Acta Cryst. A* **25** (4) (1969) 508.
- [28] R. Horisaki, R. Egami & J. Tanida, “Single-shot phase imaging with randomized light (SPIRaL)”. *Opt. Express* **24**, 37653773 (2016).
- [29] X. Huang, H. Yang, R. Harder, Y. Hwu, I.K. Robinson & Y.S. Chu, “Optimization of overlap uniformness for ptychography,” *Opt. Express* **22** (2014), 12634-12644.
- [30] J. Hunt, T. Driscoll, A. Mrozack, G. Lipworth, M. Reynolds, D. Brady, and D. R. Smith, ”Metamaterial Apertures for Computational Imaging,” *Science* **339** (2013), 310-313.
- [31] Y. Jiang, Z. Chen, Y. Han, P. Deb, H. Gao, S. Xie, P. Purohit, M. W. Tate, J. Park, S. M. Gruner, V. Elser & D. A. Muller “Electron ptychography of 2D materials to deep sub-angstrom resolution,” *Nature* **559** 343-349 (2018).
- [32] C. Kohler, F. Zhang and W. Osten, “Characterization of a spatial light modulator and its application in phase retrieval,” *Appl. Opt.* **48** (2009) 4003-4008.
- [33] A.P. Konijnenberg, W.M.J. Coene and H.P. Urbach, “Model-independent noise-robust extension of ptychography,” *Opt. Exp.* **26** (2018) 5857-5874.
- [34] C. Kuang, Y. Ma, R. Zhou, J. Lee, G. Barbastathis, R. R. Dasari, Z. Yaqoob & P.T.C. So, “Digital micromirror device-based laser-illumination Fourier ptychographic microscopy,” *Opt. Exp.* **23**(2015), 26999-27010.
- [35] G. Lipworth, A. Mrozack, J. Hunt, D.L. Marks, T. Driscoll, D. Brady, ”Metamaterial apertures for coherent computational imaging on the physical layer,” *J. Opt. Soc. Am. A* **30** (2013), 1603-1612.
- [36] A. M. Maiden, M. J. Humphry, F. Zhang and J. M. Rodenburg, “Superresolution imaging via ptychography,” *J. Opt. Soc. Am. A* **28** (2011), 604-612.
- [37] A. M. Maiden, D. Johnson and P. Li, “Further improvements to the ptychographical iterative engine,” *Optica* **4** (2017), 736-745.
- [38] A.M. Maiden, G.R. Morrison, B. Kaulich, A. Gianoncelli & J.M. Rodenburg, “Soft X-ray spectromicroscopy using ptychography with randomly phased illumination,” *Nat. Commun.* **4** (2013), 1669.
- [39] A.M. Maiden & J.M. Rodenburg, “An improved ptychographical phase retrieval algorithm for diffractive imaging,” *Ultramicroscopy* **109** (2009), 1256-1262.
- [40] A. M. Maiden, J. M. Rodenburg and M. J. Humphry, “Optical ptychography: a practical implementation with useful resolution,” *Opt. Lett.* **35** (2010), 2585-2587.
- [41] J. Miao, D. Sayre, and H. N. Chapman. “Phase retrieval from the magnitude of the Fourier transforms of nonperiodic objects.”, *J. Opt. Soc. Am. A* **15**(6) (1998):1662-1669.
- [42] G.R. Morrison, F. Zhang, A. Gianoncelli and I.K. Robinson, “X-ray ptychography using randomized zone plates,” *Opt. Exp.* **26** (2018) 14915-14927.
- [43] Y. S. G. Nashed, D. J. Vine, T. Peterka, J. Deng, R. Ross and C. Jacobsen, “Parallel ptychographic reconstruction,” *Opt. Express* **22** (2014) 32082-32097.
- [44] P.D. Nellist, B.C. McCallum & J.M. Rodenburg, “Resolution beyond the information limit in transmission electron microscopy, ” *Nature* **374** (1995) 630-632.
- [45] P.D. Nellist and J.M. Rodenburg, “ Electron ptychography. I. Experimental demonstration beyond the conventional resolution limits,” *Acta Cryst. A* **54** (1998), 49-60.
- [46] K.A. Nugent, “Coherent methods in the X-ray sciences, ” **59** (2010) 1-99.
- [47] X. Ou, G. Zheng and C. Yang, “Embedded pupil function recovery for Fourier ptychographic microscopy,” *Opt. Exp.* **22** (2014) 4960-4972.
- [48] X. Peng, G.J. Ruane, M.B. Quadrelli & G.A. Swartzlander, “ Randomized apertures: high resolution imaging in far field,” *Opt. Express* **25** (2017) 296187.
- [49] F. Pfeiffer, “X-ray ptychography,” *Nat. Photon.* **12** (2017) 9-17.
- [50] T. Plamann & J.M. Rodenburg, “Electron ptychography. II. Theory of three-dimensional propagation effects,” *Acta Cryst. A* **54** (1998), 61-73.
- [51] J.M. Rodenburg, “Ptychography and related diffractive imaging methods,” *Adv. Imaging Electron Phys.* **150** (2008) 87-184.

- [52] J.M. Rodenburg and H.M.L. Faulkner, “A phase retrieval algorithm for shifting illumination”. *Appl. Phys. Lett.* **85** (2004), 4795.
- [53] M.H. Seaberg, A. d’Aspremont & J.J. Turner, “Coherent diffractive imaging using randomly coded masks,” *Appl. Phys. Lett.* **107** (2015) 231103.
- [54] P. Sidorenko, O. Lahav, Z. Avnat & O. Cohen, “Ptychographic reconstruction algorithm for frequency-resolved optical gating: super-resolution and supreme robustness,” *Optica* **3** (2016) 1320-1330.
- [55] M. Stockmar, P. Cloetens, I. Zanette, B. Enders, M. Dierolf, F. Pfeiffer, and P. Thibault, “Near-field ptychography: phase retrieval for inline holography using a structured illumination,” *Sci. Rep.* **3** (2013), 1927.
- [56] D. Sylman, V. Micó, J. Garca & Z. Zalevsky, “Random angular coding for superresolved imaging,” *Appl. Opt.* **49** (2010), 4874-4882.
- [57] P. Thibault, M. Dierolf, O. Bunk, A. Menzel, F. Pfeiffer, “Probe retrieval in ptychographic coherent diffractive imaging,” *Ultramicroscopy* **109** (2009), 338-343.
- [58] P. Thibault, M. Dierolf, A. Menzel, O. Bunk, C. David, F. Pfeiffer, “High-resolution scanning X-ray diffraction microscopy”, *Science* **321** (2008), 379-382.
- [59] P. Thibault and M. Guizar-Sicairos, “Maximum-likelihood refinement for coherent diffractive imaging”. *New J. Phys.* **14** (2012), 063004.
- [60] L. Tian, Z. Liu, L-H Yeh, M. Chen, J. Zhong, L. Waller, “Computational illumination for high-speed in vitro Fourier ptychographic microscopy,” *Optica* **2** 904-911 (2015).
- [61] L. Valzania, T. Feurer, P. Zolliker & E. Hack, “Terahertz ptychography,” *Opt. Lett.* **43** (2018), 543-546.
- [62] C. M. Watts, D. Shrekenhamer, J. Montoya, G. Lipworth, J. Hunt, T. Sleasman, S. Krishna, D. R. Smith, and W. J. Padilla, “Terahertz compressive imaging with metamaterial spatial light modulators,” *Nat. Photon.* **8** (2014), 605-609.
- [63] L. Yeh, J. Dong, J. Zhong, L. Tian, M. Chen, G. Tang, M. Soltanolkotabi, and L. Waller, “Experimental robustness of Fourier ptychography phase retrieval algorithms,” *Optics Express* **23** (2015) 33214-33240.
- [64] F. Zhang, B. Chen, G. R. Morrison, J. Vila-Comamala, M. Guizar-Sicairos & I. K. Robinson, “Phase retrieval by coherent modulation imaging,” *Nat. Comm.* **7** (2016):13367.
- [65] F. Zhang, G. Pedrini & W. Osten, “Phase retrieval of arbitrary complex-valued fields through aperture-plane modulation,” *Phys. Rev. A* **75** (2007), 043805.
- [66] X. Zhang, J. Jiang, B. Xiangli, G.R. Arce, “Spread spectrum phase modulation for coherent X-ray diffraction imaging,” *Optics Express* **23** (2015), 25034-25047.
- [67] Y. Zhang, P. Song, Q. Dai, “Fourier ptychographic microscopy using a generalized Anscombe transform approximation of the mixed Poisson-Gaussian likelihood,” *Opt. Exp.* **25** (2017) 168-179.
- [68] G. Zheng, R. Horstmeyer and C. Yang, “Wide-field, high-resolution Fourier ptychographic microscopy,” *Nature Photonics* **7** (2013), 739-745.
- [69] C. Zuo, J. Sun and Q. Chen, “Adaptive step-size strategy for noise-robust Fourier ptychographic microscopy,” *Optics Express* **24** (2016), 20724-20744.

DEPARTMENT OF MATHEMATICS, UNIVERSITY OF CALIFORNIA, DAVIS, CALIFORNIA 95616, USA. EMAIL: FANNJIANG@MATH.UCDAVIS.EDU

DEPARTMENT OF MATHEMATICS, UNIVERSITY OF CALIFORNIA, DAVIS, CALIFORNIA 95616, USA.